Rational design, synthesis and evaluation of ZnO nanorod array supported Pt:La$_{0.8}$Sr$_{0.2}$MnO$_3$ lean NO$_x$ traps

Shoucheng Du[a,b,1], Sibo Wang[a], Yanbing Guo[a,b], Xingxu Lu[a], Wenxiang Tang[a], Yong Ding[c], Xuefei Mao[d], Pu-Xian Gao[a,*]

[a] Department of Materials Science and Engineering & Institute of Materials Science, University of Connecticut, Storrs, Connecticut 06269-3136, USA
[b] 3D Array Technology LLC, Storrs, Connecticut 06269, USA
[c] School of Materials Science and Engineering, Georgia Institute of Technology, Atlanta, GA 30332, USA
[d] Institute of Quality Standard and Testing Technology for Agro-Products, Chinese Academy of Agricultural Sciences, and Key Laboratory of Agro-food Safety and Quality, Ministry of Agriculture, Beijing 100081, PR China

A B S T R A C T

In this study, a new type of lean NO$_x$ traps (LNT) based on Pt:La$_{0.8}$Sr$_{0.2}$MnO$_3$ (LSMO) nanoparticles decorated on ZnO nanorod array integrated monoliths have been successfully designed and demonstrated. Compared to the commercial catalyst, the nanorod array based catalyst demonstrates competitive NO oxidation activity, and exceptional hydrothermal stability and recoverability after sulfur poisoning. With uniform distribution of perovskite and Pt nanoparticles, the ZnO nanorod array retains its structure after long-time exposure to the reducing gaseous atmosphere. The H$_2$ treatment induces the surface Mn^{4+} reduction to Mn^{3+} and subsequently to Mn^{2+}, affecting oxygen mobility, and decreasing the amount of surface lattice oxygen on the LSMO perovskite, thus leading to the catalyst performance decay according to a Mars-Van Krevelen reaction mechanism. Such surface state change was found to be reversible, with the catalytic performance fully recovered after O$_2$ re-treatment, making it suitable for NO$_x$ storage and reduction (NSR). The complete lean NO$_x$ traps are formulated with rationally-designed sequential BaCO$_3$ and Pt loading, improving NOx storage capacity. The ZnO nanorod array supported LNT shows good water compatibility under simulated exhaust. The nanorod array catalysts may be potentially suitable for vehicular NO$_x$ emission control.

1. Introduction

Lean-burn engines with excessive air/fuel ratio (A/F > 20) are attractive in their improved combustion efficiency, contributing to advantageous fuel economy [1–3]. However, it also generates obstacles for aftertreatment of the emissions, especially nitrogen oxides (NO$_x$) [4–6]. A lean NO$_x$ trap (LNT) or a NO$_x$ storage and reduction (NSR) catalyst is one of the most promising technologies for NO$_x$ removal from the lean-burn exhausts under the excessive oxygen conditions [7–9]. Generally, the LNT stores NO$_x$ as nitrates (or nitrite) during the lean conditions, and releases the stored NO$_x$ for selective reduction to N$_2$ during the short rich conditions [10,11].

Typical NSR catalysts consist of three major components including precious metals (e.g., Pt, Pd, Rh) as oxidation/reduction catalysts, alkali or alkaline earth metal oxides (e.g., Ba, Sr, Ca, Li, K, or Na) as NO$_x$ storage materials, and a transition metal oxide (e.g., γ-Al$_2$O$_3$) as catalyst support [12–15]. The use of Pt is to enhance NO oxidation to NO$_2$ and facilitate the storage process, as NO$_2$ is more favorable to be adsorbed by the storage materials such as BaCO$_3$, compared to NO. However, due to high cost and low thermal durability of Pt, alternatives such as perovskite [16,17] have drawn attentions to replace the Pt-based LNT catalysts.

The ABO$_3$ –type perovskite oxides, where A designates a rare-earth or alkaline earth cation and B a transition metal cation, are attractive because of their ease of synthesis, low cost, and high thermal stability [16,18]. The La-based perovskite oxides, such as LaCoO$_3$, LaMnO$_3$, and LaNiO$_3$, have tunable catalytic properties by substituting a small fraction of A-site atoms with other cations such as Ba, Ce, or Sr [18–20]. The Sr doped La-based perovskite has been studied as promising NO oxidation and NO$_x$ storage catalysts. Kim et al. [18] developed different perovskite-based catalysts for diesel oxidation and NO$_x$ storage and reduction. They observed that substituting Sr into La-based perovskites

was efficient in increasing NO oxidation performance, making them potentially good alternatives to the Pt-based catalysts. Constantinou et al. [9] also studied Sr-based perovskite LNT catalysts, which showed good NO to NO_2 conversion and NO_x storage ability. Incorporating perovskite with Pt not only lowered Pt usage and the associated cost, but also increased the catalytic oxidation activity [21–23].

A typical method for making industrial monolithic catalysts is through a washcoating technology [24–26], where Pt based [27–29] or perovskite based [9,18] LNT catalysts in powder form are synthesized first and then washcoated onto the monolithic substrate channel surfaces. Recently, we have developed a new approach to integrate the catalysts with the monolithic substrate through in situ nanostructure forest growth onto channel surfaces (Figure S1) [30–33]. The geometry (e.g. shape, length and population) of the catalysts (nanorod arrays) can be well controlled by the synthesis conditions [34,35]. The well-defined geometries have opened possibilities to build precise structure–property correlations for the catalysts, enabling enhanced performance by optimizing the catalyst structures [36,37]. Compared with the conventional washcoated monolithic catalysts, the unique geometrical and spatial arrangements of the nanorod arrays can reduce catalyst usage by a factor of 10–40 while maintaining or excelling at good catalytic activity and thermal/mechanical robustness [30,31]. The nanorod array geometry also greatly benefits the dispersion of precious metals, thus providing more options for selecting metal oxide types, without being restricted by the high surface area but sulfur affinity γ-Al_2O_3 support [38]. The nanorod array based catalysts have demonstrated excellent performance on catalytic removal of CO and HCs. However, their application for NO_x emission control has not been reported so far.

Herein, we developed the perovskite nanorod array based full LNT formulation, including NO oxidation catalyst, NO_x reducing catalyst, and NO_x storage materials, for the first time and demonstrated its NO_x removal performance under practical exhaust condition including 10% water vapor. Specifically, we have successfully designed and synthesized a set of nanorod array based monolithic catalysts by integrating honeycomb substrate with ZnO nanorod arrays, LSMO, Pt and $BaCO_3$. The nanorod array catalysts have shown comparable NO oxidation activity to the commercial catalyst[2] with better hydrothermal stability. The recoverability from sulfur and reducing gas poisoning enables the potential of the catalysts for practical use. Moreover, the ZnO nanorod arrays demonstrate better water resistance than the alumina support used in the commercial catalyst. It is hoped that the current work brings new approaches for design, synthesis and integration of LNT catalysts. The results based on the well-defined nanorod array structures could provide insights for the general catalysis research on the NO_x storage and reduction.

2. Experimental section

2.1. Materials synthesis

The whole synthesis process is schematically illustrated in Fig. 1. To prepare ZnO seeding solution, 2.19 g zinc acetate dihydrate (Zn(Ac)$_2$·H$_2$O) was dissolved in 500 ml ethanol for 20 mM [Zn^{2+}] ethanol solution. A clean cordierite honeycomb substrate (600 psi, Corning Inc.) of the dimension of 6.35 cm (diameter) × 2.54 cm (channel length) was submerged in the seeding solution and sonicated for 1 min. The substrate was immediately dried under microwave irradiation. The submerging-drying step was repeated 10 times until the desired quantity of the precursor was deposited onto the substrate. The material was then calcined in a furnace at 350 °C for 2 h to obtain crystallized ZnO seeds.

Growth of ZnO nanorod arrays on the cordierite monolith substrate was carried out in a continuous flow reactor. Equal moles of zinc acetate and hexamethylenetetramine (HMT) (6.25 mM each) were dissolved in 2000 ml DI water for a precursor solution. The monolith substrate was vertically mounted in a quartz tube reactor. The precursor solution was driven by a peristaltic pump to steadily flow through the substrate channels. The flow rate was 150 sccm and the reactor was kept at 95 °C in water bath for 6 h. After growth of ZnO nanorod arrays, the sample was rinsed with DI water and dried in an electrical oven at 90 °C overnight.

LaSrMnO$_3$ perovskite was deposited onto ZnO nanorod arrays using a microwave-assisted wash-coating method. First, a perovskite type sol-gel solution was prepared by dissolving stoichiometric lanthanum(III) nitrate hexahydrate, strontium nitrate, manganese(II) nitrate tetrahydrate and tetraamineplatinum(II) nitrate in 20 ml N, N-Dimethylformamide (DMF) under sonication. Another solution was made by dissolving 2 g polyvinylpyrrolidone (M.W. 55,000 g/mol) and 0.5 ml diethanolamine in 20 ml DMF. The two solutions were then mixed under vigorous stirring at 60 °C and the solution rapidly turned dark brown. After 24 h' aging, a piece of ZnO nanorod array sample was submerged in the sol-gel solution under sonication. The sample was then transferred to a microwave oven for drying. This deposition process was repeated for multiple cycles until the desired loading amount ((mass of sample after perovskite loading - mass of sample before perovskite loading)/mass of sample before perovskite loading = 15 wt%, ~30 g/l monolith catalyst) was acquired. The final calcination was carried out at 700 °C for 2 h with the heating rate of 5 °C/min. The Sr to La doping molar ratio was 2:8, verified by inductively coupled plasma optical emission spectrometry (ICP-OES).

Pt nanoparticles were loaded either with perovskite using a sol-gel method, or after perovskite and $BaCO_3$ loading using an impregnation method. In the sol-gel method, tetraammineplatinum(II) nitrate (2.4 mM) was added into the perovskite sol-gel solution prior to aging, and then the same deposition procedure was followed as described above. The final Pt concentration was around 6.6 g/l total in the prepared structured catalyst (analyzed by ICP-OES). Catalysts with relatively high Pt concentration were developed in this study, mainly because of their good hydrothermal stabilities, compared to those with low Pt concentration (Figure S2). In the impregnation method, the tetraammineplatinum(II) nitrate was dissolved in DI water forming a precursor solution. The sample after perovskite and $BaCO_3$ loading was fully dipped into the solution and then dried at 80 °C. The process was repeated several times until all the solution was consumed.

Deposition of $BaCO_3$ nanoparticles includes two steps. First, $BaCO_3$ nanoparticles were synthesized through a sonication-assisted replacement reaction. 0.005 mol Ba(NO$_3$)$_2$ and 0.005 mol NaCO$_3$ were mixed in 50 ml ethylene glycol. The solution was ultrasonicated at 80 °C for 1 h. The acquired $BaCO_3$ nanoparticles were collected and rinsed in DI water. In the second step, the as-prepared $BaCO_3$ nanoparticles were dispersed in ethanol and deposited on the sample using a sequential washcoating method. The $BaCO_3$ mass loading ratio was controlled to be ~7 wt% (verified by ICP-OES) of the total sample.

Overall, in this study, we are interested in designing ZnO nanorod array based $La_{0.8}Sr_{0.2}MnO_3$ catalysts (written as ZnO/LSMO) with Pt and $BaCO_3$ decoration following different integration sequences. The catalysts included in this study are ZnO/LSMO, ZnO/LSMO/Pt, ZnO/LSMO/Pt/BaCO$_3$, and ZnO/LSMO/Pt/BaCO$_3$/Pt. The components from the left to the right in the above sample names divided by the slash symbols represent their loading sequences from the beginning to the end. LSMO/Pt refers to co-deposition of LSMO and Pt.

2.2. Materials characterization

The X-ray diffraction (XRD) patterns of the prepared catalysts were acquired using a BRUKER D2 X-ray diffractometer (Cu Kα radiation, λ = 1.540598 Å) with an operating voltage of 30.0 keV, and a beam

---

[2] Disclaimer: a fully formulated automotive catalyst is designed to perform at a high level over its full useful life in the presence of occasional extreme temperature excursions, exposure to fuel and oil-related poison and contaminant species, repeated cold-start and shut-down cycles, etc.. Experiments on model catalysts do not normally address all of those issues or operating modes.
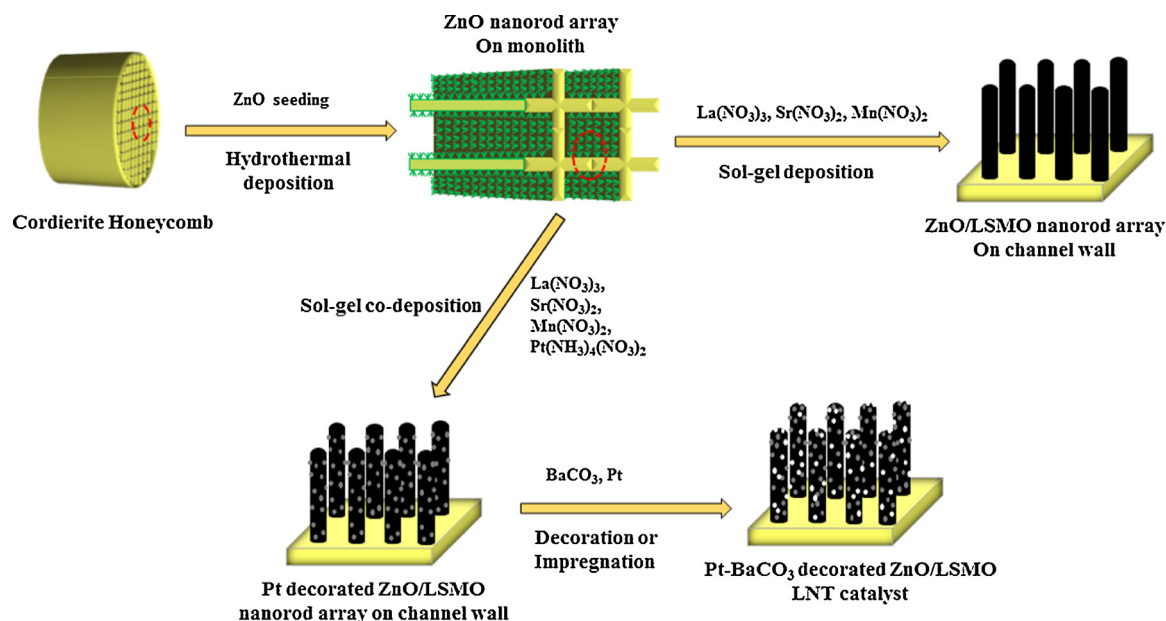
Fig. 1. A schematic flow diagram of the nanorod array LNT catalyst synthesis process.

current of 10 mA. The morphology and structure of nanorod array catalysts were characterized using a field-emission scanning electron microscope (SEM) (FEI Nova NanoSEM 450) at an accelerating voltage of 15.0 keV, and a high-resolution scanning transmission electron microscope (STEM) (FEI Talos F200X S/TEM, 200 kV). The cross-sectional (S)TEM samples were characterized under a Tecnai 30 STEM at an accelerating voltage of 300.0 keV. Both high resolution TEM and high angle annular dark field (HAADF) imaging modes were used under the STEM. In order to prepare the cross-section (S)TEM samples, the samples were sandwiched by two pieces of Si wafer using conductive epoxy. After two hours' baking at 100 °C, the samples were polished from both sides to reach 100 microns in thickness. The samples were further dimple grinded to 20 microns, and then ion milled until a small hole appeared at the center of each sample.

H_2-temperature programmed reduction (H_2-TPR) was carried out in a ChemiSorb 2720 Pulse Chemisorption System. Each catalyst was placed in the reactor without pretreatment in hydrogen. The catalyst was heated from 30 °C to 800 °C at a heating rate of 10 °C/min under 25 sccm gas flow of 4% H_2 balanced in N_2. Surface states of the catalysts were characterized using a Kratos Analytical (Axis Ultra DLD) X-ray photoelectron spectrometer (XPS). The X-ray radiation was generated by a monochomatic Al Kα source operating at photon energy of 1486.7 eV. The signal of photoelectron was filtered by a hemispherical analyzer with pass energy of 100 eV and 30 eV for survey scan and high-resolution scan, respectively. C1 s photoelectron line at 284.6 eV was adopted as internal standard for spectra calibration to compensate the charging effect. The bulk content of each element contained in the synthesized catalysts was determined by ICP-OES (Optima 2000DV, Perkin Elmer). The samples were ground and dissolved into 10 ml aqua regia at 90 °C for 15 h. Then hydrofluoric acid (HF) of 2 ml was added for further dissolving the solid. The whole solution was diluted to 25 ml and ready for ICP-OES analysis.

2.3. Catalyst performance evaluation

NO oxidation performance of the catalysts was evaluated in a horizontal quartz tube reactor. Catalyst of the volume of 0.8 cm × 0.8 cm × 1 cm was loaded, and wrapped with insulation wools to fix the position in the reactor and enforce the flow going through the monolith channels. The inertness of the insulation wool was confirmed by experiments. A K-type thermocouple was inserted

into the reactor for on-line measurement of the actual catalyst temperature. The concentrations of NO (200 ppm), O_2 (8%), and N_2 (balanced) were controlled using mass flow controllers. The total gas flow rate was 500 sccm to maintain ~47, 000 h^{-1} space velocity. Fourier Transform infrared spectrometer (FTIR, Thermo-fisher Nicolet 6700), calibrated for NO and NO_2, was used for on-line gas analysis. At the beginning of the experiment, the furnace was maintained at 80 °C. The inlet reactant gases were bypassing the catalyst. Each experiment was initiated by starting the furnace, the Omnic software and the temperature recorder, and switching the gases to the catalyst at the same time. The catalysts after hydrothermal aging and sulfur poisoning were re-tested under the same conditions as was used for the fresh ones. Commercial benchmark lean NO_x trapping (LNT) catalyst from Umicore with a Platinum Group Metals (PGM) loading of about 3 g/l was also evaluated for comparison.

Catalytic NO_x storage and reduction was performed in a specially designed fixed bed reactor (Fig. 2). The whole reactor setup contains a multi-gas delivery system consisted of four mass flow controllers, a horizontal tube furnace, an on-line temperature recorder connected to a K-type thermocouple, a steam generator, and a FTIR calibrated for NO, NO_2, CO and CO_2 for on-line gas analysis. In each experiment, catalyst of the volume of 0.8 cm × 0.8 cm × 3 cm was used. The total gas flow rate was maintained at 1500 sccm for ~47, 000 h^{-1} space velocity. The NSR experiments were performed at 300 °C in this study. The experiment was initiated at lean condition (200 ppm NO, 10% O_2, and 10% CO_2) for 300 s and switched to rich condition (200 ppm NO, 1% H_2, 3% CO, and 10% CO_2) for 120 s. A relatively long rich time was used to obtain more data points and more easily evaluate the reactions occurring during the rich period [9]. Four cycles of lean-rich switching were performed for each catalyst. All the experiments in this study were performed following a protocol developed in the US Driving Research and Innovation for Vehicle Efficiency and Energy Sustainability (US DRIVE) workshop [39] and summarized in Table 1.

3. Results and discussion

3.1. Characterizations of the nanorod array catalysts

By the hydrothermal synthesis method, nanorod arrays were grown on the cordierite substrate with well controlled full coverage of the whole substrate (Fig. 3 (a)). The length of the nanorod array was about
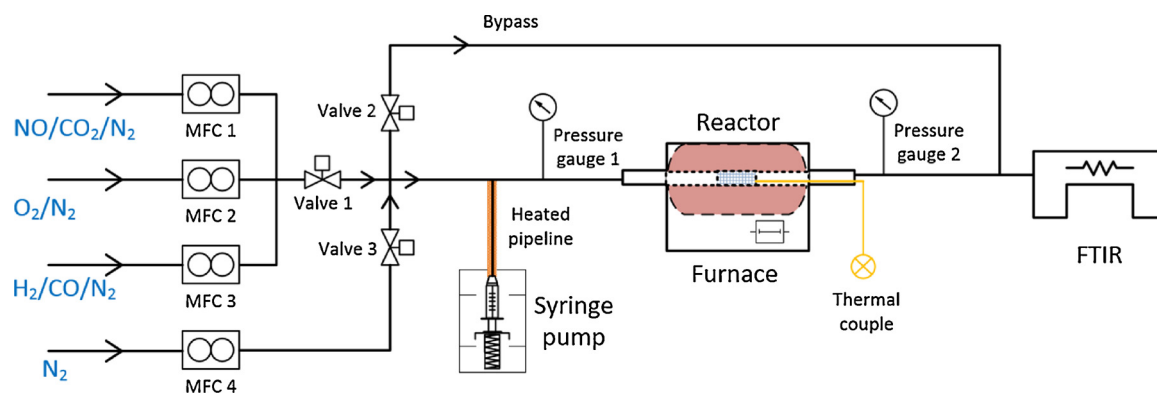
Fig. 2. Specially designed reactor setup for NO_x storage and reduction with the capability of computer controlled switching between lean and rich conditions.

6 µm (Fig. 3 (c)). Homogeneous nucleation of ZnO was not observed from the SEM images, meaning that it was successfully suppressed with the synthesis approach developed in a continuous flow reactor. The ZnO nanorod array exposes the hexagonal (0001) plane as seen from the top view SEM image (Fig. 3 (b)), suggesting that the growth direction of ZnO along [0001] direction [35].

The perovskite catalysts alone typically show low sulfur resistance and require relatively high temperature for reduction of adsorbed sulfur compounds during rich condition, both of which can be effectively improved by integration of platinum-group metals (PGM) [18,40]. In addition, integrating Pt with perovskite could further enhance both NO oxidation and NSR activities [11]. For these reasons, we have developed Pt-enhanced LSMO catalyst on the ZnO nanorod array. The TEM image and corresponding EDX analysis along the cross-section (Fig. 3 (d, f)) and at the "O_1" point of the outer surface (Fig. 3 (d, e)) of the nanorod array confirm that the nanorod array has ZnO nanowire core with LSMO thin film (~5 nm) and Pt coated on the outer surface.

Elemental mapping (Fig. 3 (h–k)) confirms the uniform elemental distribution of ZnO/LSMO/Pt core-shell structure. La and Mn of the LSMO perovskite are distributed along the ZnO nanorod array, with randomly distributed Sr detected due to its low concentration. Pt nanoparticles of about 1 ~ 2 nm in size are uniformly dispersed on the ZnO nanorod array (Fig. 3 (g, k)). Overall, SEM and TEM characterizations qualitatively confirm the successful growth of ZnO nanorod array on three-dimensional monolithic cordierite substrate with uniformly distributed LSMO and Pt on the ZnO nanorod array. Quantitative analysis of the materials loading was performed using ICP, as shown in Table 2. ZnO/LSMO/Pt/BaCO$_3$/Pt has 2.9 g/l Pt impregnated after BaCO$_3$ loading in addition to the 6.6 g/l Pt co-deposited with LSMO. The

relatively large difference of LSMO loading in ZnO/LSMO and ZnO/LSMO/Pt represent the inhomogeneity of different sample locations selected for ICP analysis or the errors generated during sample preparation in ICP analysis.

3.2. NO oxidation activity

Previous work has shown that NO_2 adsorbs on NO_x storage materials more efficiently than NO, which suggests that NO oxidation (NO to NO_2 conversion) is a critical step in improving the overall performance of a LNT catalyst. Thus, in this study, NO oxidation performances of ZnO/LSMO and ZnO/LSMO/Pt nanorod array catalysts were evaluated first. NO oxidation rates were measured as a function of temperature from 180 to 250 °C before the reaction reaches thermodynamic limitation (Fig. 4 (a)). From the FTIR spectra analysis (not shown here), NO and NO_2 were the only gas components detected, and no N_2O or any other side products were observed. Reaction rates over all three catalysts decrease with increasing temperature, resulting in negative apparent activation energies ($-22.4–24.9$ kJ/mol). ZnO/LSMO exhibits 7% higher NO oxidation rate than the commercial benchmark LNT. Pt incorporation into ZnO/LSMO has further enhanced the oxidation rate by 12%, compared to the commercial LNT.

The turn-over frequency (TOF) over LSMO on ZnO nanorod array was also compared to that over LSMO coated on the Al_2O_3 support reported by Kim et al. [18] and LMO powders by Chen et al. [41], to study the effect of the array configuration. As shown in Fig. 4 (b), the LSMO in the nanorod array catalyst has contributed to about 34% higher TOF than the LSMO in the alumina supported powder-form catalyst and three times higher than the LMO powder catalyst, which is

Table 1
Summary of experimental conditions.

| Cycle mode	Temp. (°C)	Duration	Exhaust make-up (N_2 balance)						
			O_2	CO_2	H_2O	CO	H_2	NO	SO_2
NOx storage and reduction condition									
Lean	300	300 s	10%	10%	(10%)[a]			200 ppm	
Rich	300	120 s	10%	10%	(10%)[a]	3%	1%	200 ppm	
NO oxidation condition									
Ramp at 2 °C/min	100–600		8%					200 ppm	
Hydrothermal aging condition									
Lean	800	50 h	10%	5%	5%				
Sulfur poisoning condition									
Pretreat	600	0.3 h	12%		6%				
Cool	600–300		12%		6%				
Poison	300	5 h	12%	6%	6%	300 ppm	100 ppm	120 ppm	3 ppm
Cool	300–100		12%		6%				
Desulfation recovery condition									
Rich	700	0.5 h				3%	1%		

[a] Wet condition applies to Fig. 10 (b).
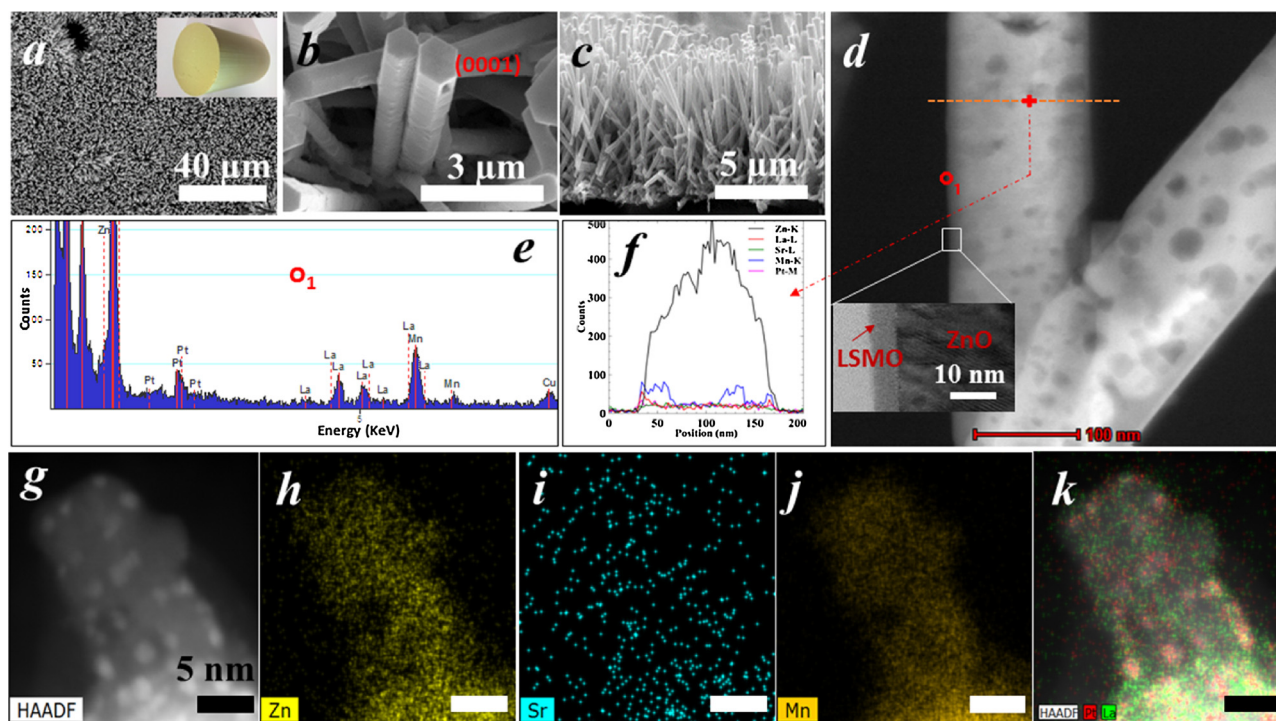
Fig. 3. (a, b) Top view and (c) side view SEM images of ZnO/LSMO nanorod arrays grown on a monolith substrate (inset in (a)). (d) STEM image of a ZnO/LSMO/Pt nanorod array and corresponding EDX spectrum (e) at the point of the outer surface and line-scan profile (f) along the cross-section. The inset of (d) is a zoomed-in bright field image of LSMO and ZnO interface. (g) A HAADF TEM image and (h–k) the corresponding elemental maps of a ZnO/LSMO/Pt nanowire. Scale bars: 5 nm.

Table 2
ICP characterization of the synthesized nanorod array catalysts.

Samples	ZnO loading (g/L)	LSMO loading (g/L)	Pt loading (g/L)	BaCO$_3$ loading (g/L)
ZnO/LSMO	87.3	25.4	–	–
ZnO/LSMO/Pt	87.3	29.2	6.6	–
ZnO/LSMO/Pt/ BaCO$_3$/Pt	106.7	28.6	9.5	50.7

attributed to the enhanced LSMO dispersion on the array structure (Fig. 3) as well as the oxygen vacancies generated by strontium doping. The high TOF of the nanorod array catalyst further implies that by applying the nanorod array structure, the usage of the active materials

can be reduced while maintaining comparable catalytic activity to the powder-from catalysts.

3.3. Hydrothermal stability and sulfur resistance

Prior to hydrothermal aging, the ZnO/LSMO/Pt nanorod array catalyst shows comparable overall NO oxidation performance to the commercial Pt based catalyst (Fig. 5). It should be noted that in this study, the catalytic performance of the in-house developed nanorod array catalysts is directly compared to that of the commercial catalyst, with different PGM loadings given the single PGM (Pt) loaded in the array versus the mixed PGM (Pt, Pd, and Rh) in the commercial catalyst. The significant different composition of the nanorod array catalyst and the commercial catalyst has made the exact performance
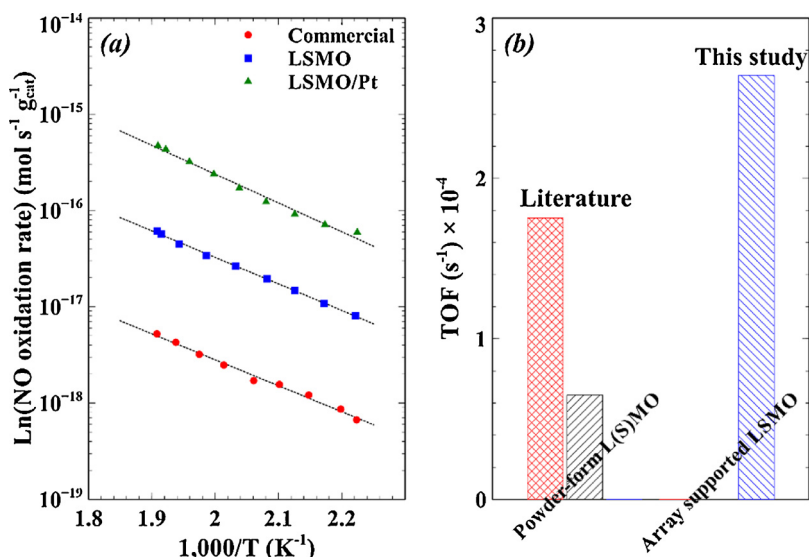

Fig. 4. (a) Arrhenius plots of the forward NO oxidation rates over the fresh nanorod array catalysts, compared to the commercial benchmark. When calculating the reaction rate, the mass of the monolith substrate was included. Conditions: 200 ppm NO + 8% O$_2$, 500 sccm, 0.8 cm × 0.8 cm × 1 cm monolithic catalyst volume, 180–250 °C. (b) Comparison of turn-over frequencies (TOF) per mol L(S)MO over powder-form L(S)MO catalysts [18,41] and ZnO nanorod array supported LSMO catalyst.
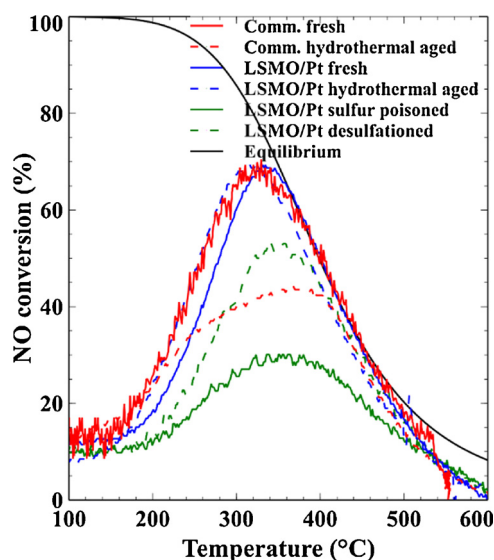
Fig. 5. NO oxidation over ZnO/LSMO/Pt catalysts before and after hydrothermal aging and sulfur poisoning. The thermodynamic equilibrium curve was calculated with an RGibbs reactor in Aspen Plus. Helium was used as the balance gas for simulation instead of N_2 to avoid any N_2 involved thermodynamic reactions.

comparison difficult. But it is true that incorporating perovskite with Pt (ZnO/LSMO/Pt) indeed enhances the activity of the catalyst with the same Pt loading (ZnO/Pt), as perovskite promotes Pt dispersion and stability during hydrothermal aging [42]. At temperatures below 350 °C, the conversions are relatively low but increase with temperature. After 350 °C, the conversion begins to drop due to the thermodynamic limitation and the reaction then follows the calculated thermodynamic equilibrium curve [43].

After hydrothermal aging, the nanorod array catalyst exhibits steadily stable NO oxidation activity, while the commercial catalyst has about 20% conversion decay. Collapse of the alumina support structure and the resulting decreased surface area in the commercial catalyst during high temperature sintering process is one of the main reasons for catalyst deactivation during oxidation of engine exhaust [44]. On the contrary, the ZnO nanorod array maintains its structure integrity after aging (Figure S3). Moreover, the interfaces between ZnO and perovskite may help immobilize the perovskite coating and prevent the agglomeration of perovskite nanoparticles.

The STEM/HAADF images of the cross-sectional samples milled from nanorod array monolithic catalyst before and after hydrothermal aging are illustrated in Fig. 6. Some Pt particles aggregation was observed in the aged sample, which however well retained the core-shell nano-array structures, showing a good hydrothermal stability. This also coincides with the well-retained low temperature NO oxidation activity in the conversion curve of the nanorod array catalyst (dashed blue in Fig. 5) after hydrothermal aging.

The effect of sulfur was also studied on the nanorod array catalyst. After sulfur poisoning, the maximum NO conversion of nanorod array catalyst drops from 68% to below 30%. The performance decay caused by sulfur might be attributed to formation of sulfates on Pt and further spillover of the sulfates to perovskite [40]. After desulfation in the reducing gas atmosphere, the conversion is recovered to about 50%, suggesting partial decomposition of sulfates [18,40,45]. This further means that sulfates do not lead to complete collapse of the LSMO structure and irreversible loss of catalytic activities.
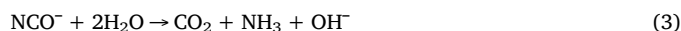
3.4. Stability and recoverability in reducing gas

In this study, we examined the stability of the perovskite structure

in the reducing gaseous atmosphere and its capability of recovery after switching to the lean condition. We performed NSR over the three types of nanorod array catalysts in the forms of fresh, hydrogen-treated, and hydrogen treated with oxygen recovery. We have focused on the stability of the nanorod array and the perovskite without Pt and storage materials loading because the perovskite structure was known to be vulnerable to frequent exposure to reducing environment [18].

Fig. 7 (a) shows four lean/rich cycles over fresh ZnO/LSMO nanorod array catalyst. In the lean condition of the first cycle, the NO oxidation activity is greater than that in the subsequent cycles. The same scenario is also seen with the H_2 treated and the O_2 recovered catalysts. This could be because the surface state of LSMO is slightly changed by the reducing gas exposure, which is verified by XPS and elaborated in the later section. This impact is amplified by exposing to H_2 for longer time (Fig. 7 (b)). From the second cycle, NSR over the nanorod array catalyst reaches steady state, demonstrating about 45% NO oxidation conversion in the lean cycle. NO_2 storage is clearly better than NO storage, although the total NOx storage capacity is low because ZnO/LSMO does not possess storage materials (See [3,26] for details about interpretation of the NSR results).

When switching to the rich cycle, the stored NO_2 is completely reduced, while the stored NO is released to the gas phase, seen from the NO spikes during switching. The appearance of the spikes is reminiscent of the spikes found with the barium-containing LNT catalyst by reaction of the NO_x stored on the barium sites, adjacent to the Pt sites, with CO adsorbed on the Pt sites via CO spillover from the Pt sites to the barium sites [46]. The overall surface chemistry on the ZnO/LSMO/Pt nano-arrays may be proposed to follow the following reactions (1)–(4).

$$H_2 + CO_2 = H_2O + CO \tag{1}$$

$$CO + NO_3^- \rightarrow NCO^- + 3CO_2 \tag{2}$$

$$NCO^- + 2H_2O \rightarrow CO_2 + NH_3 + OH^- \tag{3}$$

$$2NCO^- + H_2O + 3O_2 \rightarrow 2CO_2 + NO + NO_2 + 2OH^- \tag{4}$$

The origin of CO was proposed to be from the Reaction (1), reverse water-gas shift reaction (rWGS) [46]. Formation of isocyanate species (NCO^-) on the catalyst surface is achieved by CO spillover from the Pt sites to the barium sites where NOx is adsorbed as NO_3^- (Reaction (2)) [47,48]. H_2O and O_2 compete for further conversion of NCO^-, producing NH_3 via Reaction (3) and NO_x via Reaction (4) (NO_2 is re-adsorbed on LSMO, but NO is released), respectively. In ZnO/LSMO (Fig. 7 (a)), the NO spikes during switching are smaller than those in barium-containing nanorod array based LNT catalyst (Fig. 9 (e)), mainly because of low NO_x storage capacity of ZnO/LSMO. However, the existence of the NO spikes in ZnO/LSMO may suggest that ZnO/LSMO alone has some extent of storage capability in both NO_x and CO associated with its oxygen storage capacity [49–51].

In the rich cycle, about 20% of the NO either released from the catalyst surface or originally in the gas phase is reduced. 3% CO is introduced at the beginning of the rich cycle and the concentration maintains during the rich period. At this point, we do not know if part of CO reacts with NO_x, because even if ppm CO is consumed by NOx reduction, the trivial change in concentration is probably not able to be observed from FTIR. But in literature it is reported that NO_x is primarily reduced by H_2 when H_2 and CO co-exist [47]. Concentration of CO_2 does not change when the condition is switched from lean to rich.

After exposure to the reducing gas for 1 h, the NO oxidation activity of the fresh ZnO/LSMO in the lean cycle is significantly deteriorated (Fig. 7 (b)). However, NO and NO_2 reduction activities in the rich cycle are not affected by hydrogen treatment. After exposure to oxygen, the NO oxidation activity of ZnO/LSMO in the lean cycle is fully recovered (Fig. 7 (c)).

Change of the ZnO/LSMO bulk structure in the reducing gas atmosphere was examined by XRD (Fig. 8 (a)). Generally, the bulk structure of ZnO/LSMO is maintained in hydrogen treatment, although
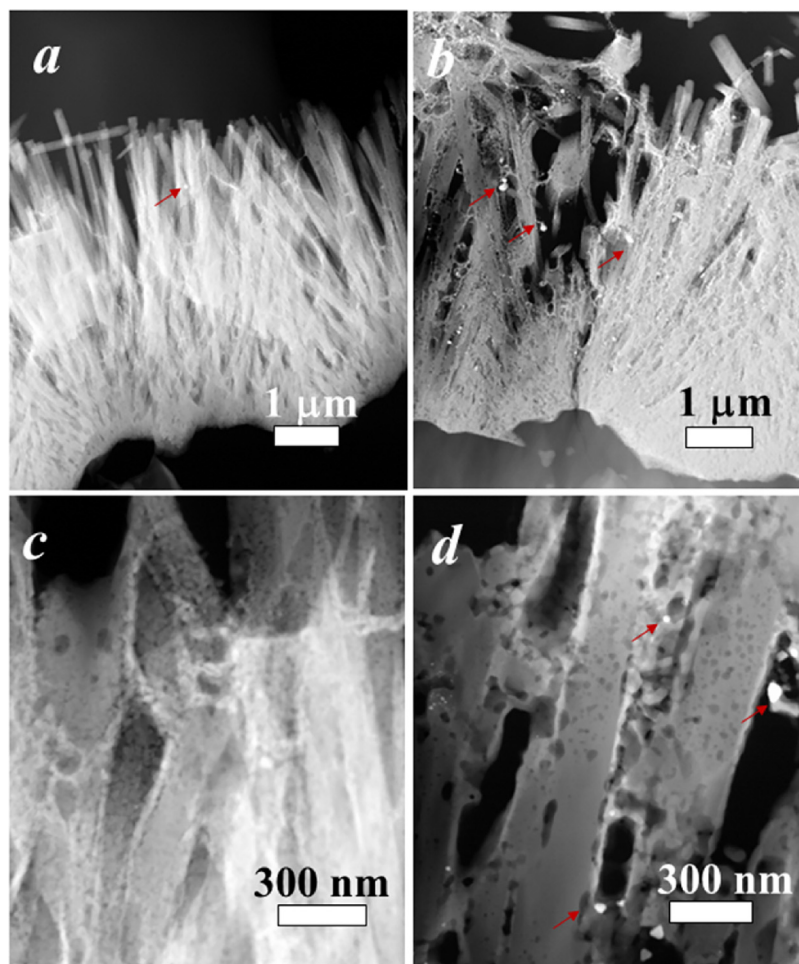
Fig. 6. STEM/HAADF images of cross-sectionally milled ZnO/LSMO/Pt nanorod array catalysts (a, c) before and (b, d) after hydrothermal aging. Red arrows in b) and d) point to the scattered agglomerated Pt particles after hydrothermal aging. (For interpretation of the references to colour in this figure legend, the reader is referred to the web version of this article).
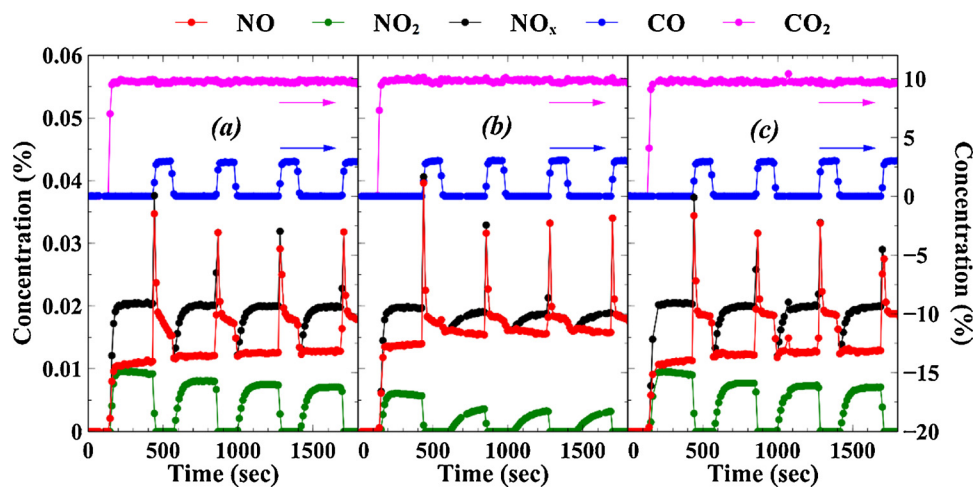

Fig. 7. Stability of ZnO/LSMO nanorod arrays in the reducing environment. 4-cycle NSR performance tested at 300 °C over nanorod array structures of (a) ZnO/LSMO, (b) ZnO/LSMO after H_2 treatment at 300 °C for 1 h, (c) ZnO/LSMO after h_2 treatment at 300 °C for 1 h, and then O_2 recovery at 600 °C.

the intensity of ZnO is reduced to some extent due to partial reduction of the ZnO nanorod array. After oxygen treatment, the intensity of ZnO is fully recovered, meaning that metallic Zn due to reduction of ZnO does not evaporate to the gas stream but remains on the array structure. The robust bulk structure of ZnO/LSMO shows its potential to be employed as LNT catalyst.

The performance decay of ZnO/LSMO after hydrogen treatment might be related to the surface structural change of the catalyst, as verified by XPS investigations. As shown in Fig. 8 (b), O 1s spectra could be deconvoluted into five peaks representing oxygen species contributed from H_2O, CO_2, ZnO, surface adsorbed oxygen (before adsorption, it is an oxygen vacancy) (O^-), and surface lattice oxygen
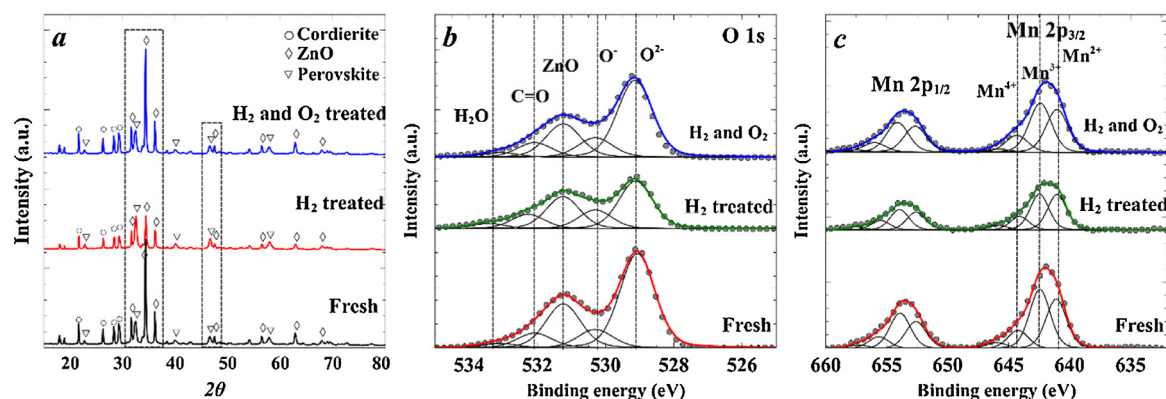
Fig. 8. (a) XRD and (b, c) XPS spectra of ZnO/LSMO before and after H_2 treatment at 300 °C for 1 h, and after O_2 recovery at 600 °C.

(O^{2-}), respectively. The thickness of the perovskite coating can be estimated to be ~5 nm from the inset of Fig. 3 (d), right at the edge of the XPS detection depth. Thus, it is possible that the perovskite coating is thick enough to prevent XPS detection of ZnO. For this, the survey scan mode (Figure S4) was applied to confirm ZnO detection and its contribution to the O 1 s spectra. As summarized in Table 3, surface lattice to surface adsorbed oxygen ratio decreases after H_2 treatment, meaning that surface lattice oxygen is preferentially reduced in the reducing atmosphere, whereas surface adsorbed oxygen is less affected by H_2 treatment. Decrease of the lower binding energy peak (lattice oxygen [52]) by H_2 treatment was also observed by Li et al. [40] with Pd doped $La_{0.7}Sr_{0.3}CoO_3$ catalyst. The performance decay in NO oxidation observed here may be due to the decrease of surface lattice oxygen, in coincidence with the Mars-Van Krevelen mechanism proposed for CO [53] and hydrocarbon oxidation [54] over perovskite catalysts. As such, NO may react with and is therefore affected by the surface lattice

Table 3
Surface XPS analysis and conversion results of ZnO/LSMO nanorod arrays.

	$O_{lattice}/O_{ads}$	Mn^{4+}/Mn^{3+}	Mn^{3+}/Mn^{2+}	Oxidation Conv. (%)
Fresh	5.12	0.31	1.20	39.5
H_2 treated	2.56	0.38	1.01	22.0
H_2 treated/O_2 recovered	4.11	0.34	1.14	38.5

oxygen, leaving an oxygen vacancy on the surface of catalyst, which will be refilled by oxygen in gas phase or lattice oxygen in bulk. Such a refill process may be affected by the Mn surface state changes.

In Fig. 8 (c), Mn 2p spectra were deconvoluted into four peaks, namely Mn^{2+}, Mn^{3+}, Mn^{4+} and a very small satellite peak [55,56], although absence of Mn^{2+} was reported in other literature [41,57,58].
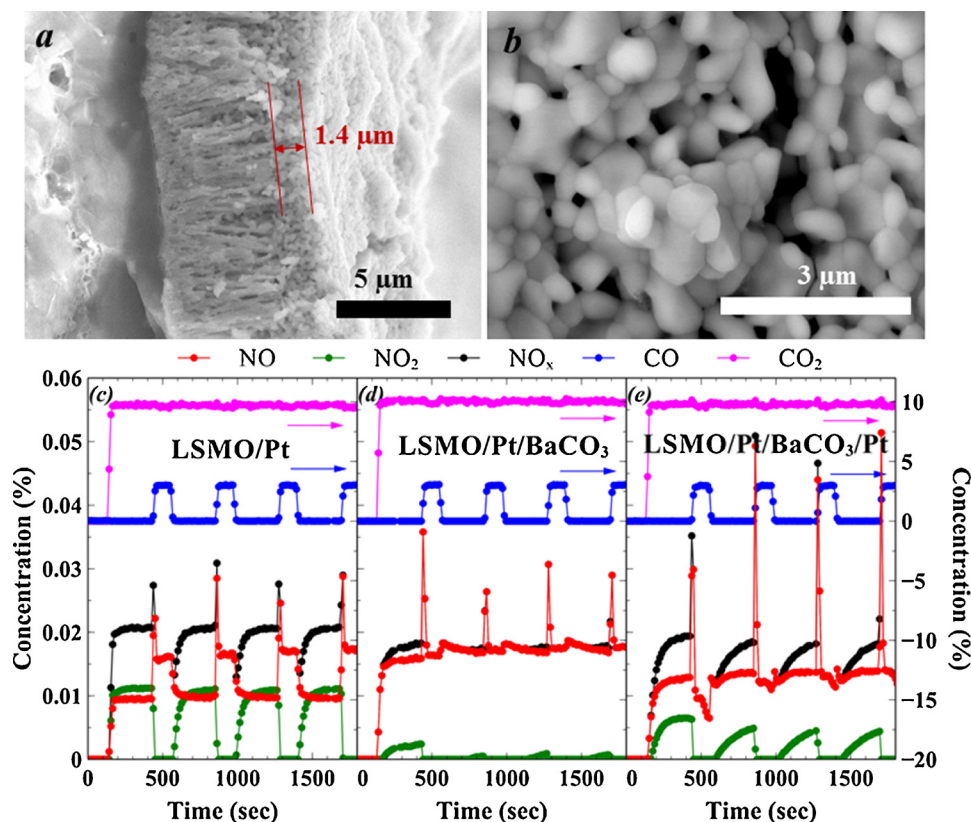

Fig. 9. (a) Cross-sectional and (b) top view SEM images of ZnO/LSMO/Pt/BaCO₃ nanorod array catalysts. 4-cycle NSR performance tested at 300 °C over nanorod array structures of : (c) ZnO/LSMO/Pt, (d) ZnO/LSMO/Pt/BaCO₃, and (e) ZnO/LSMO/Pt/BaO₃/Pt.

Mn^{4+} is reduced to Mn^{3+}; Mn^{3+} to Mn^{2+} by H_2, represented by an increase of Mn^{4+}/Mn^{3+} ratio and a decrease of Mn^{3+}/Mn^{2+} ratio in Table 3. The increase of Mn^{4+}/Mn^{3+} ratio during reduction means the amount of Mn^{3+} reduced to Mn^{2+} is greater than the amount of Mn^{4+} reduced to Mn^{3+}. Reduction of Mn^{4+} to Mn^{3+} and subsequently to Mn^{2+} during H_2 treatment of La-based perovskites is consistent with the observations from Li and Lin [21]. Change of the surface state of Mn from Mn^{4+} to Mn^{3+} and Mn^{2+} decreases the oxygen mobility from the bulk to the surface, which could be another reason for NO oxidation performance decay [41].

After oxygen exposure, Mn^{2+} is re-oxidized to Mn^{4+} and Mn^{3+} to a certain extent, together with the almost fully recovered NO oxidation conversion. Overall, the surface states of the LSMO perovskite (mainly Mn and lattice oxygen) are affected during long-time exposure to H_2, which contributes to NO oxidation performance decay. But the oxidation activity of the perovskite can be recovered by re-oxidation of the catalyst, which enables maintaining of active surface sites of the LSMO perovskite during regular lean/rich cycles.

3.5. NO_x storage and reduction

With good NSR stability in the reducing environment and good NO oxidation performance, the ZnO/LSMO/Pt nanorod array catalyst was integrated with the NO_x storage materials forming a complete LNT catalyst. $BaCO_3$ was chosen as the storage material in this study, because of its high thermal stability in the presence of CO_2 [11,59]. We examined the effect of $BaCO_3$ loading on the ZnO/LSMO nanorod array. A 7 wt% $BaCO_3$ loading on the ZnO/LSMO/Pt nanorod array catalyst results in full coverage on the array structure, with about 1.4 µm thickness above the array structure (Fig. 9 (a)). $BaCO_3$ nanoparticles are initially distributed in between of the nanorod arrays, and then when the interspace of nanorod arrays is filled up, $BaCO_3$ starts to accumulate on top of the nanorod arrays, forming relatively dense surface layer on top of the array structure (Fig. 9 (b)).

By comparing Fig. 9 (a) with Fig. 7 (a), it is clear that Pt incorporation increases both NO oxidation conversion in the lean condition and NO_x reduction, especially NO reduction in the rich condition. As the NO_x storage component, $BaCO_3$ loading significantly affects NO oxidation performance as well as the catalysts' NO_x storage capacity (Fig. 9 (c) and (d)). This is either because of $BaCO_3$ nanoparticles coverage over the LSMO and Pt active sites causing sites poisoning, or attributed to the limited mass transport of the gaseous species to the LSMO and Pt active sites. Blockage of the accessible pores by Ba-component deposition was also observed in the powder-form catalysts on ceria, silica, or alumina support [28,60], usually resulting in decrease of the surface area. However, as nanorod array catalysts are less porous compared to the typical mesoporous alumina support in the powder washcoated catalysts, the blockage effect of $BaCO_3$ loading seems to be much more significant than the powder washcoated catalysts. A systematic study on the effect of $BaCO_3$ loading on the nanorod array catalysts' NSR performance, especially NO oxidation performance, is summarized in **Figure S5**, where 40% $BaCO_3$ loading completely deteriorates NO oxidation activity of the catalyst.

Therefore, it is necessary to explore the various deposition configurations of ZnO/LSMO nanorod array catalysts. An alternative configuration is to load $BaCO_3$ prior to Pt, based on the hypothesis that the exposed Pt sites can maintain good NO oxidation activity. The effect of loading 2.87 g/l Pt after $BaCO_3$ is shown in Fig. 9 (e). Clearly in this configuration, loading Pt outside $BaCO_3$ improves NO oxidation activity and NO_x storage capacity as Pt is not covered by $BaCO_3$ and has closer contact with Ba sites [61]. The exposed Pt enhances adsorption of oxygen and reducing gases (H_2 or hydrocarbons) under lean and rich conditions, respectively. The closer contact between Pt and Ba sites promotes spillover of the adsorbed oxygen and reducing gases from the Pt sites to the nearby Ba sites, reacting with the adsorbed NO_x [62]. The NO spikes seen when switching from lean to rich condition are much

greater in ZnO/LSMO/Pt/BaO_3/Pt than ZnO/LSMO/Pt/$BaCO_3$. This also implies better Pt functionality in adsorbing CO (from rWGS) and $BaCO_3$ functionality in adsorbing NO_x in ZnO/LSMO/Pt/BaO_3/Pt catalyst, as having been discussed in Section 3.4.

However, it is noted that the perovskite, which is supposed to contribute to NO oxidation performance significantly, is to some extent covered by $BaCO_3$. Moreover, the dispersion of Pt particles on $BaCO_3$ might not be as good as that on nanorod array, diluting the functionality of the array structure. Moreover, NO_x storage capacity of 0.83 µmol NO_2/g and 0.18 µmol NO/g was obtained with this configuration, which has not been comparable to the benchmark catalyst yet. To improve the NO_x storage capacity, it is important to mitigate the $BaCO_3$ coverage, increase $BaCO_3$ adsorption efficiency, and decrease the mass loading of the $BaCO_3$. A proposed possible approach to achieve this is to synthesize small sized $BaCO_3$ particles [63] to enhance more interaction with Pt nanoparticles once loaded.

3.6. Water compatibility

Water has been shown to have complicated effects over the NSR reactions in LNT catalysts. On the one hand, NO_x adsorption and storage was known to be negatively affected by water at the operating temperature of 300 °C [64,65]. Szanyi et al. [66] found that water slows down the NO_x uptake as it decreases the contact between the active storage phase (BaO) and the Pt nanoparticles where NO_2 is being formed. By forming large Ba-nitrate particles, the diffusion of NO_2 into the bulk is also slowed down. However, the total amount of already adsorbed NO_x is not affected by the presence of water (They performed NOx adsorption prior to introducing water). In a more practical situation where NO_x and water are co-fed to the catalyst, competitive adsorption exists. For instance, Toops et al. [67] reported that 5% water could decrease the surface nitrate storage by 92% on Al_2O_3 supported LNT catalyst as a result of hydroxyl groups formation on the Al_2O_3 surface, leading to fewer vacant sites for NO_x adsorption. On the other hand, the reduction of stored NO_x, in the presence of CO_2, is shown to be promoted by water. Luo and Epling [46] proposed a model on the Pt/Ba/Al_2O_3 NSR catalyst, suggesting CO formed from rWGS (reaction (1) in Section 3.4) can negatively affect regeneration of the catalyst, due to the unfavorable cycle between barium isocyanates and nitrates (Reaction (2) and (4)). Adding water could thermodynamically suppresses rWGS (Reaction (1)) and enhances the reaction (3), forming NH_3. Both could promote NO_x reduction.

To look into the water effect on the ZnO/LSMO/Pt/$BaCO_3$/Pt nanorod array catalyst, we performed NSR experiments under both dry and wet conditions (Fig. 10). Quantitatively, the existence of water in the feed decreases NO oxidation conversion by 3%, from 24% to 21%, and reduces the NO_x (mainly NO_2) storage capacity by 25%, from 1.01 µmol/g catalyst to 0.76 µmol/g catalyst, due to the competition of water to the NO_x storage sites [68]. It should be noted that the general water effect on NO_x storage is identical between Al_2O_3 based typical NSR catalyst and the ZnO nanorod array based NSR catalyst. However, the decrease of the NO_x capacity of the nanorod array catalyst in the presence of water is much smaller than that of the Al_2O_3 supported catalyst [67], showing another advantage of using nanorod arrays as the catalyst support for NSR.

The effect of water on NO_x reduction with the nanorod array based catalyst is to certain extent inconclusive, as in both dry and wet conditions, NO_2 is fully reduced with negligible NO reduction. However, while comparing the third and fourth lean-rich cycles, the smaller NO spikes in the wet condition might suggest that water enhances the reaction (3), forming NH_3 which is quickly consumed by NO_x, and competitively suppresses the reaction (4), where the released NO_2 is restored on the barium sites while the released NO escapes from the catalyst surface (shown as spikes). This is quite consistent with the water effect observed with Al_2O_3 based model NSR catalyst.
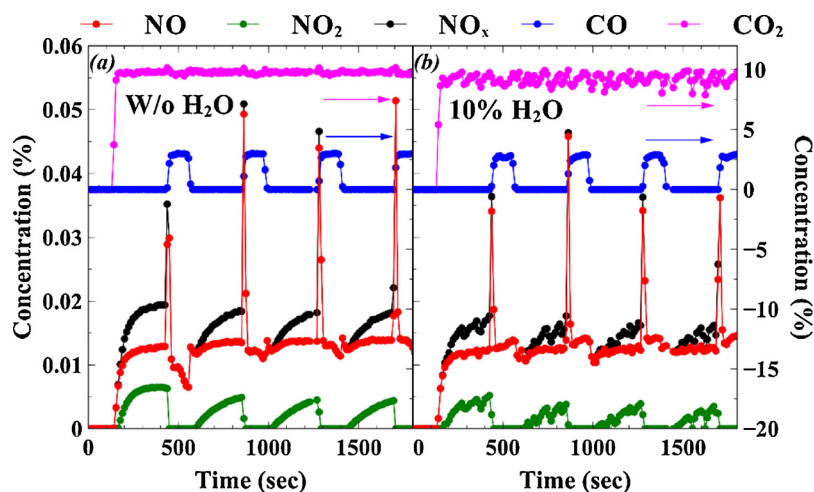
Fig. 10. (a, b) The effect of water (10%) on a 4-cycle NSR performance tested at 300 °C over ZnO/LSMO/Pt/BaCO$_3$/Pt.

4. Conclusions

In this study, we have successfully demonstrated a nanorod array based LNT catalyst for NO$_x$ reduction. Specifically, ZnO nanorod array based Pt enhanced La$_{0.8}$Sr$_{0.2}$MnO$_3$ perovskite lean NO$_x$ trap catalysts were designed, synthesized and evaluated. The array structure has enhanced dispersion of LSMO, leading to superior NO oxidation activity, compared to both commercial benchmark and LSMO powder-form catalysts. The Pt enhanced perovskite catalyst demonstrated excellent hydrothermal stability and recoverable activity after sulfur poisoning in NO oxidation. The surface states of the perovskite (mainly Mn and lattice oxygen) were affected in the reducing gas atmosphere, leading to NO oxidation performance decay. However, this surface state change was reversible during the lean-rich cycles. As such, the catalytic performance was almost fully recovered in the oxidation atmosphere, exhibiting the appropriateness of using LSMO perovskite in NSR catalysts. BaCO$_3$ loading resulted in coverage of the array structure and affected NO oxidation and NO$_x$ storage performance of the ZnO/LSMO/Pt nanorod array catalyst. Loading Pt after BaCO$_3$ showed promising configuration for catalyst design, but the full utilization of the perovskite active sites and array-structure enhanced Pt dispersion merit further investigation in the near future. Water slightly reduced NO oxidation activity of the nanorod array catalyst by 3%, and decreased the NO$_x$ storage capacity by 25%, showing better water-compatibility than the classic Al$_2$O$_3$ supported LNT catalysts. This work provides an important strategy toward modeled nanorod/nanoparticle based structured catalyst design for environmental control in general.

Appendix A. Supplementary data

Supplementary material related to this article can be found, in the online version, at doi:https://doi.org/10.1016/j.apcatb.2018.05.007.

References

[1] J. Wang, Y. Ji, V. Easterling, M. Crocker, M. Dearth, R.W. McCabe, The effect of regeneration conditions on the selectivity of NOx reduction in a fully formulated lean NOx trap catalyst, Catal. Today 175 (2011) 83–92.

[2] A. Kumar, M.P. Harold, V. Balakotaiah, Isotopic studies of NOx storage and reduction on Pt/BaO/Al2O3 catalyst using temporal analysis of products, J. Catal. 270 (2010) 214–223.

[3] W.S. Epling, L.E. Campbell, A. Yezerets, N.W. Currier, J.E. Parks, Overview of the fundamental reactions and degradation mechanisms of NOx storage/reduction catalysts, Catal. Rev. 46 (2004) 163–245.

[4] B. Pereda-Ayo, D. Duraiswami, J.J. Delgado, R. López-Fonseca, J.J. Calvino, S. Bernal, J.R. González-Velasco, Tuning operational conditions for efficient NOx storage and reduction over a Pt–Ba/Al2O3 monolith catalyst, Appl. Catal. B Environ. 96 (2010) 329–337.

[5] N. Rankovic, A. Nicolle, P. Da Costa, Detailed kinetic modeling study of NOx oxidation and storage and their interactions over Pt/Ba/Al 2 O 3 monolith catalysts, J. Phys. Chem. C. 114 (2010) 7102–7111.

[6] R. Burch, J.P. Breen, F.C. Meunier, A review of the selective reduction of NOx with hydrocarbons under lean-burn conditions with non-zeolitic oxide and platinum group metal catalysts, Appl. Catal. B Environ. 39 (2002) 283–303.

[7] Y. Ji, S. Bai, M. Crocker, Al2O3-based passive NOx adsorbers for low temperature applications, Appl. Catal. B Environ. 170-171 (2015) 283–292.

[8] N.A. Ottinger, T.J. Toops, K. Nguyen, B.G. Bunting, J. Howe, Effect of lean/rich high temperature aging on NO oxidation and NOx storage/release of a fully formulated lean NOx trap, Appl. Catal. B Environ. 101 (2011) 486–494.

[9] C. Constantinou, W. Li, G. Qi, W.S. Epling, NOx storage and reduction over a perovskite-based lean NOx trap catalyst, Appl. Catal. B Environ. 134-135 (2013) 66–74.

[10] B.M. Shakya, M.P. Harold, V. Balakotaiah, Crystallite-scale model for NOx storage and reduction on Pt/BaO/Al2O3: Pt dispersion effects on NOx conversion and ammonia selectivity, Catal. Today 184 (2012) 27–42.

[11] G. Liu, P.-X. Gao, A review of NOx storage/reduction catalysts: mechanism, materials and degradation studies, Catal. Sci. Technol. 1 (2011) 552–568.

[12] R.J. Hendershot, W.B. Rogers, C.M. Snively, B.A. Ogunnaike, J. Lauterbach, Development and optimization of NOx storage and reduction catalysts using statistically guided high-throughput experimentation, Catal. Today. 98 (2004) 375–385.

[13] A. Lindholm, N.W. Currier, J. Dawody, A. Hidayat, J. Li, A. Yezerets, L. Olsson, The influence of the preparation procedure on the storage and regeneration behavior of Pt and Ba based NOx storage and reduction catalysts, Appl. Catal. B Environ. 88 (2009) 240–248.

[14] S. Roy, A. Baiker, NO x storage - reduction catalysis : from mechanism and materials properties to storage - reduction performance, Chem. Rev. 109 (2008) 4054–4091.

[15] I. Nova, L. Lietti, L. Castoldi, E. Tronconi, P. Forzatti, New insights in the NOx reduction mechanism with H2 over Pt–Ba/γ-Al2O3 lean NOx trap catalysts under near-isothermal conditions, J. Catal. 239 (2006) 244–254.

[16] S. Royer, D. Duprez, F. Can, X. Courtois, C. Batiot-Dupeyrat, S. Laassiri, H. Alamdari, Perovskites as substitutes of noble metals for heterogeneous catalysis: dream or reality, Chem. Rev. 114 (2014) 10292–10368.

[17] H.-Y. Chen, Z. Wei, M. Kollar, F. Gao, Y. Wang, J. Szanyi, C.H.F. Peden, A comparative study of N2O formation during the selective catalytic reduction of NOx with NH3 on zeolite supported Cu catalysts, J. Catal. 329 (2015) 490–498.

[18] C.H. Kim, G. Qi, K. Dahlberg, W. Li, Strontium-doped perovskites rival platinum catalysts for treating NOx in simulated diesel exhaust, Science. 327 (2010) 1624–1627.

[19] Y. Peng, W. Si, J. Luo, W. Su, H. Chang, J. Li, J. Hao, J. Crittenden, Surface tuning of La0.5Sr0.5CoO3 perovskite catalysts by acetic acid for NOx storage and reduction, Environ. Sci. Technol. 50 (2016) 6442–6448.

[20] S. Wang, Z. Ren, W. Song, Y. Guo, M. Zhang, S.L. Suib, P.-X. Gao, ZnO/perovskite core–shell nanorod array based monolithic catalysts with enhanced propane oxidation and material utilization efficiency at low temperature, Catal. Today. 258 (2015) 549–555.

[21] C.L. Li, Y.C. Lin, Methanol partial oxidation over palladium-, platinum-, and rhodium-integrated LaMnO3 perovskites, Appl. Catal. B Environ. 107 (2011) 284–293.

[22] S. Cimino, F. Donsì, G. Russo, D. Sanfilippo, Optimization of ethylene production via catalytic partial oxidation of ethane on Pt-LaMnO3 catalyst, Catal. Letters 122 (2008) 228–237.

[23] F. Donsì, S. Cimino, R. Pirone, G. Russo, D. Sanfilippo, Crossing the breakthrough line of ethylene production by short contact time catalytic partial oxidation, Catal. Today. 106 (2005) 72–76.

[24] B. Pereda-Ayo, J.A. Botas-Echevarría, J. González-Casablanca, M.P. González-Marcos, J.R. González-Velasco, Characterization of Pt and Ba over alumina wash-coated monolith for NOx storage and reduction (NSR) by FIB-SEM, Catal. Today. 216 (2013) 50–56.

[25] Y. Ji, V. Easterling, U. Graham, C. Fisk, M. Crocker, J.S. Choi, Effect of aging on the NOx storage and regeneration characteristics of fully formulated lean NOx trap catalysts, Appl. Catal. B Environ. 103 (2011) 413–427.

[26] B. Pereda-Ayo, J.R. González-Velasco, NOx storage and reduction for diesel engine exhaust aftertreatment, Diesel Engine - Combust. Emiss. Cond. Monit. InTech, 2013, pp. 161–196.

[27] S. Roy, N. van Vegten, N. Maeda, A. Baiker, NOx storage and reduction over flame-made M/MgAl2O4 (M = Pt, Pd, and Rh): a comparative study, Appl. Catal. B Environ. 119-120 (2012) 279–286.

[28] M. Piacentini, M. Maciejewski, A. Baiker, Supported Pt-Ba NOx storage-reduction catalysts: influence of support and Ba loading on stability and storage efficiency of Ba-containing species, Appl. Catal. B Environ. 66 (2006) 126–136.

[29] M. Li, V.G. Easterling, M.P. Harold, Towards optimal operation of sequential NOx storage and reduction and selective catalytic reduction, Appl. Catal. B Environ. 184 (2016) 364–380.

[30] S. Du, W. Tang, Y. Guo, A. Binder, E.A. Kyriakidou, T.J. Toops, S. Wang, Z. Ren, S. Hoang, P.-X. Gao, Understanding low temperature oxidation activity of nanoarray-based monolithic catalysts: from performance observation to structural and chemical insights, Emiss. Control Sci. Technol. (2016) 1–19.

[31] Y. Guo, Z. Ren, W. Xiao, C. Liu, H. Sharma, H. Gao, A. Mhadeshwar, P.X. Gao, Robust 3-D configured metal oxide nano-array based monolithic catalysts with ultrahigh materials usage efficiency and catalytic performance tunability, Nano Energy 2 (2013) 873–881.

[32] S. Wang, Y. Wu, R. Miao, M. Zhang, X. Lu, B. Zhang, A. Kinstler, Z. Ren, Y. Guo, T. Lu, S.L. Suib, P. Gao, Scalable continuous flow synthesis of ZnO nanorod arrays in 3-D ceramic honeycomb substrates for low-temperature desulfurization, CrystEngComm. 19 (2017) 5128–5136.

[33] S. Du, W. Tang, X. Lu, S. Wang, Y. Guo, P. Gao, Cu-decorated ZnO nanorod array integrated structured catalysts for low-pressure CO2 hydrogenation to methanol Cu-decorated ZnO nanorod array integrated structured catalysts for low-pressure CO2 hydrogenation to methanol, Adv. Mater. Interfaces (2017) 1700730.

[34] Z. Ren, Y. Guo, P.-X. Gao, Nano-array based monolithic catalysts: concept, rational materials design and tunable catalytic performance, Catal. Today. 258 (2015) 441–453.

[35] S. Wang, Z. Ren, Y. Guo, P.-X. Gao, Nano-array integrated monolithic devices: toward rational materials design and multi-functional performance by scalable nanostructures assembly, CrystEngComm. 18 (2016) 2980–2993.

[36] Z. Ren, V. Botu, S. Wang, Y. Meng, W. Song, Y. Guo, R. Ramprasad, S.L. Suib, P.-X. Gao, Monolithically integrated spinel MxCo3−xO4 (M = Co, Ni, Zn) nanoarray catalysts: scalable synthesis and cation manipulation for tunable low-temperature CH4 and CO oxidation, Angew. Chemie Int. Ed. 53 (2014) 7223–7227.

[37] Z. Ren, Z. Wu, W. Song, W. Xiao, Y. Guo, J. Ding, S.L. Suib, P.-X. Gao, Low temperature propane oxidation over Co3O4 based nano-array catalysts: Ni dopant effect, reaction mechanism and structural stability, Appl. Catal. B Environ. 180 (2016) 150–160.

[38] F.C. Galisteo, R. Mariscal, M.L. Granados, M.D.Z. Poves, J.L.G. Fierro, V. Kroger, R.L. Keiski, Reactivation of sulphated Pt/Al2O3 catalysts by reductive treatment in the simultaneous oxidation of CO and C3H6, Appl. Catal. B Environ. 72 (2007) 272–281.

[39] The Advanced Combustion and Emission Control (ACEC) Technical Team, Characterization and Performance Evaluation: Low-Temperature Oxidation Catalyst Test Protocol, (2015).

[40] X. Li, C. Chen, C. Liu, H. Xian, L. Guo, J. Lv, Z. Jiang, P. Vernoux, Pd-doped perovskite: an effective catalyst for removal of NOx from lean-burn exhausts with high sulfur resistance, ACS Catal. 3 (2013) 1071–1075.

[41] J. Chen, M. Shen, X. Wang, G. Qi, J. Wang, W. Li, The influence of nonstoichiometry on LaMnO3 perovskite for catalytic NO oxidation, Appl. Catal. B Environ. 134-135 (2013) 251–257.

[42] S. Wang, S. Du, W. Tang, S. Hoang, X. Lu, W. Xiao, B. Zhang, J. Weng, E. Schneer, Y. Guo, J. Ding, Z. Zhang, P.-X. Gao, Mesoporous perovskite nanotube-array enhanced metallic-state platinum dispersion for Low temperature propane oxidation, ChemCatChem. 10 (2018) 1–7.

[43] J.A. Loiland, R.F. Lobo, Oxidation of zeolite acid sites in NO/O2 mixtures and the catalytic properties of the new site in NO oxidation, J. Catal. 325 (2015) 68–78.

[44] Y.X.E. Rodrigues, N.F.A. Matynia, T.A.P. Rodatz, Aging of commercial diesel oxidation catalysts: a preliminary structure / reactivity study, Top. Catal. 59 (2016) 1039–1043.

[45] S. Poulston, R.R. Rajaram, Regeneration of NOx trap catalysts, Catal. Today 81 (2003) 603–610.

[46] J.Y. Luo, W.S. Epling, New insights into the promoting effect of H2O on a model Pt/Ba/Al2O3 NSR catalyst, Appl. Catal. B Environ. 97 (2010) 236–247.

[47] H. Abdulhamid, J. Dawody, E. Fridell, M. Skoglundh, A combined transient in situ FTIR and flow reactor study of NOx storage and reduction over M/BaCO3/Al2O3 (M = Pt, Pd or Rh) catalysts, J. Catal. 244 (2006) 169–182.

[48] T. Szailer, J.H. Kwak, D.H. Kim, J.C. Hanson, C.H.F. Peden, J. Szanyi, Reduction of stored NOx on Pt/Al2O3 and Pt/BaO/Al2O3 catalysts with H2 and CO, J. Catal. 239 (2006) 51–64.

[49] J.L.G. Fierro, L. González Tejuca, Kinetics of CO adsorption on the perovskite-type oxide LaCrO3, J. Colloid Interface Sci. 96 (1983) 107–114.

[50] B. Abrahamsson, H. Grönbeck, NO x adsorption on ATiO3 (001) perovskite surfaces, J. Phys. Chem. C. 119 (2015) 18495–18503.

[51] S. Hodjati, K. Vaezzadeh, C. Petit, V. Pitchon, A. Kiennemann, Absorption/desorption of NOx process on perovskites: performances to remove NOx from a lean exhaust gas, Appl. Catal. B Environ. 26 (2000) 5–16.

[52] J. Kuhn, U. Ozkan, Surface properties of Sr- and Co-doped LaFeO3, J. Catal. 253 (2008) 200–211.

[53] P.D. Petrolekas, I.S. Metcalfe, Solid electrolyte potentiometric study of La(Sr)Mno3 catalyst during carbon-monoxide oxidation, J. Catal. 152 (1995) 147–163.

[54] S. Royer, H. Alamdari, D. Duprez, S. Kaliaguine, Oxygen storage capacity of La1-xÀxBO3 perovskites (with À = Sr, Ce; B = Co, Mn)— relation with catalytic activity in the CH4 oxidation reaction, Appl. Catal. B, Environ. 58 (2005) 273–288.

[55] B. Zhao, R. Ran, L. Sun, X. Guo, X. Wu, D. Weng, NO catalytic oxidation over an ultra-large surface area LaMnO3 + δ perovskite synthesized by an acid-etching method, RSC Adv. 6 (2016) 69855–69860.

[56] W. Si, Y. Wang, Y. Peng, J. Li, Selective dissolution of A-site cations in ABO3 perovskites: a New path to high-performance catalysts, Angew. Chem. - Int. Ed. 54 (2015) 7954–7957.

[57] C. Zhang, C. Wang, W. Zhan, Y. Guo, Y. Guo, G. Lu, A. Baylet, A. Giroir-Fendler, Catalytic oxidation of vinyl chloride emission over LaMnO3 and LaB0.2Mn0.8O3 (B = Co, Ni, Fe) catalysts, Appl. Catal. B Environ. 129 (2013) 509–516.

[58] Y. Liu, H. Dai, Y. Du, J. Deng, L. Zhang, Z. Zhao, C.T. Au, Controlled preparation and high catalytic performance of three-dimensionally ordered macroporous LaMnO3 with nanovoid skeletons for the combustion of toluene, J. Catal. 287 (2012) 149–160.

[59] J.Y. Luo, M. Meng, X.G. Li, Y.Q. Zha, Highly thermo-stable mesoporous catalyst Pt/BaCO3-Al2O3 used for efficient NOx storage and desulfation: comparison with conventional impregnated catalyst, Microporous Mesoporous Mater. 113 (2008) 277–285.

[60] V. Labalme, N. Benhamou, N. Guilhaume, E. Garbowski, M. Primet, Modifications of Pt/alumina combustion catalysts by barium addition I. Properties of fresh catalysts, Appl. Catal. A Gen. 133 (1995) 351–366.

[61] R. Büchel, R. Strobel, F. Krumeich, A. Baiker, S.E. Pratsinis, Influence of Pt location on BaCO3 or Al2O3 during NOx storage reduction, J. Catal. 261 (2009) 201–207.

[62] P.T. Fanson, M.R. Horton, W.N. Delgass, J. Lauterbach, FTIR analysis of storage behavior and sulfur tolerance in barium-based NOx storage and reduction (NSR) catalysts, Appl. Catal. B Environ. 46 (2003) 393–413.

[63] M.O. Symalla, A. Drochner, H. Vogel, R. Büchel, S.E. Pratsinis, A. Baiker, Structure and NOx storage behaviour of flame-made BaCO3 and Pt/BaCO3 nanoparticles, Appl. Catal. B Environ. 89 (2009) 41–48.

[64] L. Lietti, P. Forzatti, I. Nova, E. Tronconi, NO x storage reduction over Pt–Ba/γ-Al2O3 catalyst, J. Catal. 204 (2001) 175–191.

[65] W.S. Epling, G.C. Campbell, J.E. Parks, The effects of CO2 and H2O on the NOx destruction performance of a model NOx storage/reduction catalyst, Catal. Letters 90 (2003) 45–56.

[66] J. Szanyi, J.H. Kwak, D.H. Kim, X. Wang, J. Hanson, R.J. Chimentao, C.H.F. Peden, Water-induced morphology changes in BaO/gamma-Al2O3 NOx storage materials, Chem. Commun. (2007) 984–986.

[67] T.J. Toops, D.B. Smith, W.S. Epling, J.E. Parks, W.P. Partridge, Quantified NOx adsorption on Pt/K/gamma-Al2O 3 and the effects of CO2 and H2O, Appl. Catal. B Environ. 58 (2005) 255–264.

[68] L. Cumaranatunge, S.S. Mulla, A. Yezerets, N.W. Currier, W.N. Delgass, F.H. Ribeiro, Ammonia is a hydrogen carrier in the regeneration of Pt/BaO/Al2O3 NOx traps with H2, J. Catal. 246 (2007) 29–34.